Multipactor thresholds prediction for geometries subject to standing waves

Eva Al Hajj Sleiman, Julien Hillairet, Mohamed Belhaj

Multipactor Thresholds Prediction for Geometries Subject to Standing Waves

Eva Al Hajj Sleiman[1,2], Julien Hillairet[1], Mohamed Belhaj[2]

[1]CEA, IRFM, 13108 Saint-Paul Les Durance, France
Email: eva.alhajjsleiman@cea.fr – Julien.hillairet@cea.fr

[2]ONERA, DPHY, Université de Toulouse, 31055 Toulouse, France
Email: Mohamed.belhaj@onera.fr

INTRODUCTION

Multipactor is a vacuum discharge, observed in microwave structures [1] at sufficiently low pressures so that the electron free path is longer than the vacuum space [2]. This discharge is caused by a resonant secondary electron emission mechanism [3], where initial electrons enter in resonance with the alternating RF field at specific phase angles. These electrons contribute to the multiplication of the number of electrons if the one-way transit time between the electrodes corresponds, roughly, to an integer number of RF cycles, so that the returning electrons see the same conditions and their velocity is large enough to liberate from electrodes' surfaces more electrons. The multipactor mechanism sustains itself also by secondary electron emission resulting from electrons' impact with the component surfaces. Multipactor can be observed in many applications such as space applications, in particular, RF satellites payloads; experimental tokamak fusion reactors RF components: antennas, transmission lines, and RF windows; microwave vacuum tubes or particle accelerator structures.

For multipactor to occur, two conditions must be simultaneously fulfilled [4]: *i)* one necessary but not sufficient condition, that the impact energy of electrons colliding with an electrode must be sufficient so that the total electron emission yield (TEEY) of the electrode surface is greater than one. *ii)* the second condition is the resonance condition for the electron's motion to be synchronized with the phase change of the RF electric field.

We are particularly interested in the case of nuclear fusion experimental devices, where the consequences of multipactor are problematic and may affect or limit the performances of the antennas used in plasma heating and current drive. This phenomenon can lead to an increase in the reflected power back to the source, which can damage the high RF power sources (klystrons or tetrodes), and therefore should be avoided. Multipactor can also trigger RF breakdowns, which can damage RF components. As multipactor experiments are expensive to realize, especially with complex components of big dimensions and for megawatts range of RF power as the ones used as heating systems for fusion reactors, we rely on numerical tools for multipactor predictions. In Ion Cyclotron plasma heating systems, the antennas used to couple the RF power to the plasma, operate at a high power density, above the highest multipactor threshold. Therefore, in practice, the multipactor power bands of the different components of the antennas are bypassed during operation. However, it requires ramping up the RF power sufficiently fast to minimize the time spent in the multipactor regions to avoid multipactor to develop and detune the RF systems [5]. This sheds the light on the importance of the determination of both the lowest and the highest multipactor thresholds of all the components of the antenna.

Contrary to other applications, such as space applications, where RF components are usually matched to the load preventing reflected power to flow back to the source, this is usually not the case for antennas used on experimental fusion reactors. These antennas are subject to high power densities under vacuum, so they are prone to multipactor regimes under a wave pattern being a resultant of incident and reflected waves. For RF frequency below the electron plasma frequencies, *i.e.* typically below 100 GHz, a mismatch can occur between the load (which is the magnetized plasma itself) and the antennas' impedance, leading to a partial power reflection. In addition, the plasma properties can change with time, thus changing the loading conditions. Moreover, there are additional causes for reflected power in the antennas due to their intrinsic RF design. For example, sections of these antennas can be resonant, meaning that the RF power recirculates within these sections. Furthermore, power splitters such as three ports passive components (T-junction type) cannot be lossless, reciprocal and mismatched at the same time; and impedance transformers, used to improve the matching to the plasma, induce some reflected power. All these component types are parts of the Ion Cyclotron antennas used on the tokamak WEST, located at Cadarache in France. Hence, it is important to determine multipactor criteria for the lowest and the highest multipactor thresholds of each component independently of the reflection coefficient values.

This paper aims to develop two criteria for the lowest and the highest (when exists) multipactor thresholds, that are independent of the amount of reflected power. Two geometries are analyzed herein: a coaxial transmission line of characteristic impedance 50 Ω, and a T-junction type component (called *bridge* hereafter) used in the IC antennas of

WEST. The rest of the paper is organized as follows; first, the previous findings on the determination of the multipactor thresholds under standing wave regimes are discussed and then the geometries' models, analyzed here, are presented. Later the methodology is explained, to finally detail the results.

PREVIOUS FINDINGS

In [6], the authors applied a computational method on quarter-wavelength coaxial lines operating under travelling, mixed and standing waves. The developed method is used to determine the multipactor powers, type and order, by following the electron trajectories in the structures. For the standing wave (SW) case, the authors start the analysis with initial electrons being seeded on both conductors. They found that, for SW, the surviving trajectories, being the electrons causing multipactor, are the ones that appear near the maximum of the electric field. Moreover, they stated that the contribution of the surviving electrons that are far from the electric field's maximum appeared at high incident powers, and the non-phase focusing electrons that are far from the electric field's maximum drift toward the minimum of the electric field. They deduced that, within their power incident range, the multipactor for coaxial lines operating in SW is due to the electric field. In addition to that, they proposed a scaling law for the electric multipactor, relating the multipactor powers of the travelling wave (TW) case (excited by a voltage V) and the SW case (excited by a voltage V from each side of the coaxial line), given by $P_{TW} = 4P_{SW}$ since the peak voltage of the SW is twice that of the TW in such a case. For the mixed wave (MW) case, they found that when the reflection coefficient increases from zero (TW case), the multipactor resonance regime is split into two distinct modes. The first set of resonance modes will coincide with the *electric* multipactor mode of the SW case. The second set of modes shifts to very high incident powers very rapidly and is caused by the magnetic field. The multipactor caused by the magnetic field is known as the *magnetic* multipactor mode. A scaling law exists between the electric multipacting powers of the MW case and the TW multipactor powers and is given by $P_{MW} \sim \frac{1}{(1+R)^2} P_{TW}$. They summarized that the multipactor for the TW case is of mixed nature where both the electric and magnetic fields contribute to multipactor, but as the reflection coefficient increases, the multipactor processes are dissociated into electric and magnetic multipactor processes. Whereas for the pure SW case, the multipactor resonance mode appears close to the maximum of the electric field, and there is no multipactor maintained at the electric field nodes. Somersalo *et al.* [6] indicate that the *magnetic* multipactor process does not exist for this case since it requires infinite incident power for it to be sustained. However, some missing multipactor processes have not been taken into account due to numerical limitations and the scanned incident power range is limited to hundreds of kW.

In [7], the authors have developed a numerical model to predict the multipactor thresholds in transverse electromagnetic (TEM) mode cylindrical coaxial transmission lines of infinite length in the propagation direction. These transmission lines are subject to three types of RF signals of different reflection coefficient $\Gamma = Re^{j\psi}$ (R and ψ are respectively the magnitude and the phase): *i)* travelling wave (TW) corresponding to a null reflection, where $R = 0$. *ii)* Mixed wave (MW) defined by a reflection coefficient of magnitude $0 < R < 1$ and phase $\psi = \pi$. *iii)* Standing wave (SW) corresponding to $R = 1$, and $\psi = \pi$. Their model was based on the computation of effective electrons' trajectories that are perturbed by the electromagnetic fields and the inter-electrons interactions to account for the space charge effect due to Coulombian repulsion. Their simulation tool allows determining the number of electrons released after each collision based on the TEEY data of the tested material. They have focused only on the lowest voltage multipactor thresholds, and have found that the voltage multipactor thresholds are higher for the SW case than the case of a TW for high values of $f \times d$ products (where f is the frequency, and d is the distance separating the inner conductor from the outer one). They attributed this effect to the existence of very low electric field regions in the wave propagation direction (SW nodes), absorbing the electrons before the ignition of the multipactor phenomenon. They found that this effect is more pronounced for $f \times d$ products higher than $7\ GHz.mm$, independently of the choice of f and d. Nevertheless, for $f \times d$ products less than this threshold the voltage multipactor thresholds are the same for SW, MW, and TW cases.

In [8], the author performed simulations of multipactor discharge using CST Particle Studio, for a coaxial waveguide subject to SW. The findings of [7] were confirmed to come from the Gaponov-Miller force that pushes electrons toward the low electric field region and contributes mitigating multipactor. In addition, three multipactor zones have been identified in the SW mode: *i)* the low electric field zones showing the similarity between the multipactor for SW and that for TW, where the Gaponov-Miller force has yet no effect; *ii)* a medium electric fields zone where this force gains strength and the secondary electrons are more concentrated in the electric field nodes; *iii)* the high electric field zones where the concentration of electrons is denser on a very small volume located in the electric field nodes. The results from Romanov's work disagreed with the analysis done by Somersalo for the SW case, since the simulations have shown a multipactor near the nodes of the electric field.

In all these papers, the multipactor thresholds were given in terms of incident RF power and reflection coefficients. In antennas for nuclear fusion experiments, however, measuring or deducing the incident and reflected powers are not always

possible, in particular in the resonant sections of the antennas. In addition, some components (such as the bridge) are not coaxial and the definition of a voltage is no more unique. Electric field topology in the components, on the contrary, can be deduced from the global circuit's model resolutions [9]. As the multipactor is inherently caused by the electromagnetic field topology inside the RF components, its knowledge is in theory sufficient to determine the multipactor susceptibility regions for a given excitation. For these reasons, multipactor thresholds are defined in the following sections in terms of electric field magnitudes rather than RF powers or voltages.

GEOMETRIES MODELS

In this paper, we address two types of geometries: a simple cylindrical coaxial cable of characteristic impedance $Z_0 = 50\ \Omega$, and the *bridge* geometry of the IC antennas used on the tokamak WEST.

Coaxial cable

We consider a uniform circular coaxial transmission line consisting of an inner conductor of radius a and an outer conductor of radius b, where $d = b - a$ is the gap spacing between electrodes (illustrated in Fig. 1). The TEM mode is considered, and the incident wave propagation direction is $+z$. At each frequency f, the length of the coaxial cable in the propagation direction is taken equal to $\lambda/2$, λ being the wavelength corresponding to frequency f. The RF electromagnetic fields are described by a superposition of two TEM waves travelling in opposite directions, *i.e.*, both ports are excited respectively with the $p\angle\psi$, and $R^2 p\angle\psi$. p being the incident power on the first port; R, and ψ respectively the magnitude and phase of the reflection coefficient $\Gamma = Re^{j\psi}$. The incident powers are normalized to 1W, leading to $p = \frac{1}{1+R^2}$. Three cases will be considered: *i)* travelling wave (TW), expressed by $R = 0$; *ii)* mixed wave (MW), expressed by $0 < R < 1$, and $\psi = 180^\circ$ (particularly we are interested in the case $R = 0.5$); and *iii)* standing wave (SW), given by $R = 1$, and $\psi = 180^\circ$. Hence, we can express the RF fields by

$$\boldsymbol{E}(\vec{r},t) = \frac{V}{\sqrt{1+R^2}rln\left(\frac{b}{a}\right)}\cos(\omega t - \beta z)\vec{e}_r + \frac{RV}{\sqrt{1+R^2}rln\left(\frac{b}{a}\right)}\cos(\omega t + \beta z + \psi)\,\vec{e}_r \quad (1)$$

$$\boldsymbol{B}(\vec{r},t) = \frac{V}{\sqrt{1+R^2}crln\left(\frac{b}{a}\right)}\cos(\omega t - \beta z)\vec{e}_\varphi - \frac{RV}{\sqrt{1+R^2}crln\left(\frac{b}{a}\right)}\cos(\omega t + \beta z + \psi)\,\vec{e}_\varphi \quad (2)$$

where $(\vec{e}_r, \vec{e}_\varphi, \vec{e}_z)$ are the unit vectors of the cylindrical coordinates (r, φ, z), $\vec{r}$ the position vector, c the light speed, $V = V_{1W} = \sqrt{2Z_0}$, and $\omega = 2\pi f$ the angular frequency.

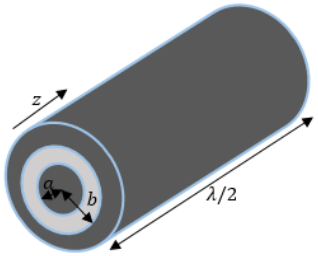

Fig. 1: Coaxial geometry representation. The light grey represents the vacuum and the dark grey the conductors.

Bridge

In experimental magnetic confined nuclear fusion reactors, radio-frequency (RF) systems are used to heat the plasma. Among the heating systems used on the tokamak WEST, is the Ion Cyclotron Resonance Heating (ICRH) system composed of three antennas operating in the frequency range [46 - 65] MHz. Each ICRH antenna, as represented in Fig. 2, is composed of two sides, left and right; each constituted of two variable capacitors, a bridge, an impedance transformer, and an RF feed-through ceramic window. Each side has its own RF power generator so that either one or both sides of the antenna could be powered. From all these components, we are particularly interested in the analysis of the multipactor properties of the bridge geometry, which is a three ports structure, as shown in Fig. 3. Since the geometry of the bridge is not homogeneous, so are the electric and magnetic fields. Therefore, the multipactor analysis region is split into six regions where geometries and fields are almost homogenous: Region D, Region E and Region F are cylindrical coaxial geometries. Whereas Region A is parallel-plates-like geometry, Region B is a coaxial geometry of elliptical cross-section and Region C is a complex geometry composed of two output ports and a parallel-plates-like geometry joining the two

ports. Practically, the incident power is only known on port 1. The incident powers on ports 2 and 3 can be obtained for a given plasma facing the antenna by modelling the circuit of the antenna with all its components: input power and phase from the generators, RF windows, impedance transformers, bridges, tuning capacitors and front face. The Table 1 gives an example of the calculated excitations for the bridge section, when the antenna is tuned to radiate without plasma, a typical case used during antenna RF conditioning. In this example, calculated at 55 MHz, the generators are set-up such that the right side is powered with (1W, 0°) and the left side with (1W, 180°).

Table 1: All bridge's port excitations were obtained from solving the antenna circuit of an IC antenna operating at 55 MHz and facing vacuum (no plasma).

Bridge side	Port#1	Port#2	Port#3
Left	(1.112W, 146.937°)	(19.081W, -143.768°)	(22.853W, 31.097°)
Right	(1.124W, -33.058°)	(35.111W, 37.49°)	(40.277W, -146.558°)

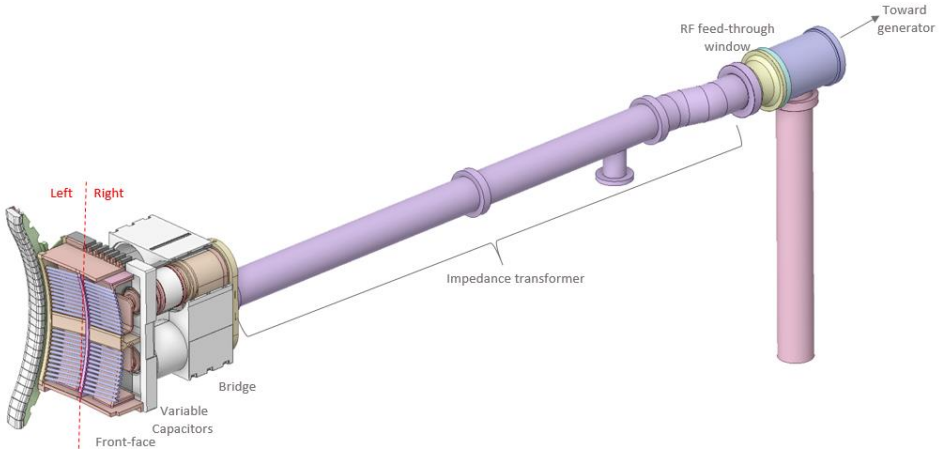

Fig. 2: An illustration of the different components of one side of an ICRH antenna used on the tokamak WEST. The other side is not shown in the figure but has the same set of components.

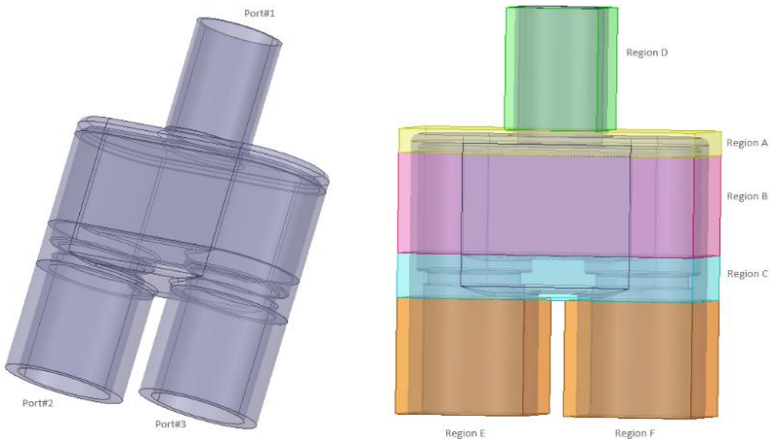

Fig. 3: Left – Bridge geometry. Right – Multipactor regions.

METHODOLOGY

To develop a criterion for each of the lower and upper multipactor powers, independently of the choice of the reflection coefficients, we first look at the case of the coaxial line. Fig. 4 represents different voltage magnitudes in function of the positions along the wave propagation direction of the coaxial cable represented in Fig. 1: *i)* the green horizontal line represents the constant voltage V, when the coaxial is subject to a TW ($R = 0$). *ii)* The orange curve represents the voltage in a coaxial cable subject to a MW with $R = 0.5$, and $\psi = 180^{\circ}$ (The voltage standing wave ration quantifying the reflected power is defined as VSWR $= \frac{V_{max}}{V_{min}} = \frac{1+R}{1-R} = 3$), so that the voltage's minimum is $\frac{V(1-R)}{\sqrt{1+R^2}}$, and the voltage maximum is $\frac{V(1+R)}{\sqrt{1+R^2}}$. *iii)* The blue curve represents the voltage in a coaxial cable subject to a SW with $R = 1$, and $\psi =$

180° (VSWR $= \infty$), so that the voltage's minimum is zero, and the voltage's maximum is $\sqrt{2}V$. The region within the dashed red lines of Fig. 4 is the multipactor region, bounded by the lower and upper voltage multipactor thresholds.

For the TW case, when $V < V_{mp,lower}$, no multipactor occurs. When $V_{mp,lower} \leq V \leq V_{mp,upper}$, the multipactor can take place anywhere in the coaxial. For the MW and SW cases, we can observe that once the peaks of the blue and orange curves reach the value $V_{mp,lower}$, the multipactor can take place in the vicinity of the maximum voltages' locations only. This reveals that the ignition of multipactor is controlled by the peak voltage on the line (i.e. peak electric field), independently of the wave pattern. Moreover, for the MW and SW cases, when the peak voltage is between $V_{mp,lower}$, and $V_{mp,upper}$ the multipactor will be triggered in the regions where the voltage is within the multipactor region as the dotted regions for the MW case. As the peak voltage is increased above the $V_{mp,upper}$, the multipactor regions get smaller as illustrated by the purple hatched regions of Fig. 4. As the peak voltage increases more above $V_{mp,upper}$, the multipactor regions move toward the minimum electric field regions. For the MW case, the multipactor will ends when the minimum voltage along the line is higher than $V_{mp,upper}$. Therefore, the multipactor region for the highest multipactor threshold will be located near the minimum electric field regions. On the contrary, for the pure SW case, the minimum voltage is always lower than $V_{mp,lower}$, while the maximum voltage can be above $V_{mp,upper}$. Hence, in theory, multipactor could always be triggered in such cases, in particular close to the nodes of the electric field. It should be noted that, in reality, due to the space charge, non-linear effects such as ponderomotive force and the surface conditioning effects (reduction of TEEY), multipactor may no more be triggered above a certain threshold, even for the pure SW case.

Motivated by this analysis, we expect that the maximum multipactor electric field corresponding to the lower power multipactor bound remains almost the same for the three wave patterns (TW, MW or SW). Moreover, we expect that the mean (average) multipactor electric field, calculated in the multipactor susceptible region, corresponding to the upper power multipactor bound remains almost the same for the three wave patterns.

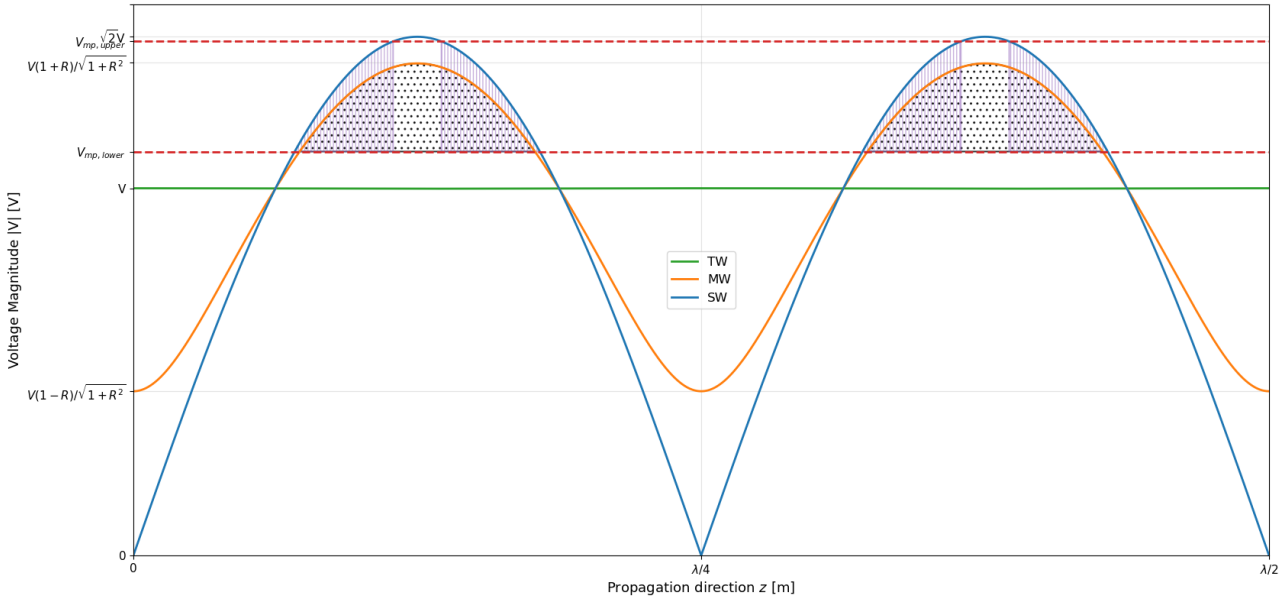

Fig. 4: Voltage magnitude at different positions of a coaxial line in the wave propagation direction. The voltages of three waves' regimes are plotted: travelling wave, mixed wave, and standing wave. The dashed red lines represent the lower and upper multipactor voltages. The dotted regions and the hatched purple regions represent respectively the multipactor locations along the propagation direction for the MW and the SW cases.

RESULTS

As a first step, the cartography of the electromagnetic fields is generated using ANSYS-HFSS for the targeted excitations' pattern $\boldsymbol{P}$ where $\boldsymbol{P}$ is the powers and phases inputs for each port of the structure. This cartography is then imported into Spark3D, which is used to determine the lower $\boldsymbol{P_{mp,lower}}$ and upper $\boldsymbol{P_{mp,upper}}$ power multipactor thresholds. As a second step, the multipactor electromagnetic field corresponding to $\boldsymbol{P_{mp,lower}}$, and $\boldsymbol{P_{mp,upper}}$ is calculated with HFSS, with the initial port excitations multiplied by the multipactor power thresholds. For $\boldsymbol{P_{mp,lower}}$, the electric field criterion is the peak multipactor electric field $E_{peak}(\boldsymbol{P_{mp,lower}})$ found in the multipactor susceptible region, located in the vicinity of the

maximum electric field. For $\boldsymbol{P_{mp,upper}}$, the electric field criterion is the mean (average) multipactor electric field $E_{mean}(\boldsymbol{P_{mp,upper}})$ calculated within the susceptible multipactor region corresponding to the upper power multipactor threshold, which is found to be a region near the lowest (nodes for the SW pattern) electric field region. The multipactor susceptible regions, corresponding respectively to $\boldsymbol{P_{mp,lower}}$ and $\boldsymbol{P_{mp,upper}}$, are the set of surface meshes where for each mesh the following inequality holds: $E_{c1} \leq E_i \times TEEY \leq E_{c2} \times TEEY_{max}$. E_{c1}, and E_{c2} are the first and second crossover energies, $TEEY_{max}$ is the maximum of the TEEY data, and $(E_i, TEEY)$ are the electrons' impact energy and average TEEY value for the surface mesh.

Coaxial cable

In Fig. 5 (left), the blue, orange and green curves represent respectively the lower and upper power multipactor thresholds ($\boldsymbol{P_{mp,lower}}$, $\boldsymbol{P_{mp,upper}}$) obtained for a 50 Ω coaxial cable in the frequency range [20 – 150] MHz, for TW, MW, and SW patterns. The purple, and black points correspond to the MW, and SW expected lower power multipactor thresholds, calculated from the TW counterpart using Somersalo's scaling laws $P_{MW} = \frac{P_{TW}(1+R^2)}{(1+R)^2}$, and $P_{SW} = \frac{P_{TW}}{2}$, since port excitations are normalized to 1W. These proposed scaling laws are in good agreement with the $\boldsymbol{P_{mp,lower}}$ obtained by simulation, as expected as this criterion is linked to the maximal electric field. The surface TEEY corresponds to that of a silver-coated stainless steel material relevant to the WEST IC operational conditions. This figure illustrates the fact that the multipactor power thresholds (lower or upper) are affected by the wave pattern, especially for the upper power multipactor thresholds. By looking at the multipactor susceptible regions for ($\boldsymbol{P_{mp,lower}}$, $\boldsymbol{P_{mp,upper}}$), it was found that the multipactor starts near the maximum (purple region) of the electric field and ends near its minimum (orange region) as depicted in the right hand sided illustration of Fig. 5. Consequently, the region chosen for the computation of the mean multipactor electric field corresponding to the upper power multipactor threshold is around the lowest electric field region (being the region of the peak of the magnetic field). The lower $E_{peak}(\boldsymbol{P_{mp,lower}})$ and upper $E_{mean}(\boldsymbol{P_{mp,upper}})$ electric field criteria corresponding to $\boldsymbol{P_{mp,lower}}$, and $\boldsymbol{P_{mp,upper}}$ are illustrated respectively in black and blue for the TW (solid lines), MW (dotted lines), and SW (dashed lines) in Fig. 6. It shows that the multipactor electric field threshold is independent of the wave pattern for both the lower and the upper thresholds, which validates the proposed criteria. The error between the peak multipactor electric field $E_{peak}(\boldsymbol{P_{mp,lower}})$ corresponding to a MW/SW case, and its TW counterpart case (taken as reference) is at most 7%. For the upper thresholds, the error between the mean multipactor electric field $E_{mean}(\boldsymbol{P_{mp,lower}})$ corresponding to a MW (SW) case, and its TW counterpart case is at most 15% (6%).

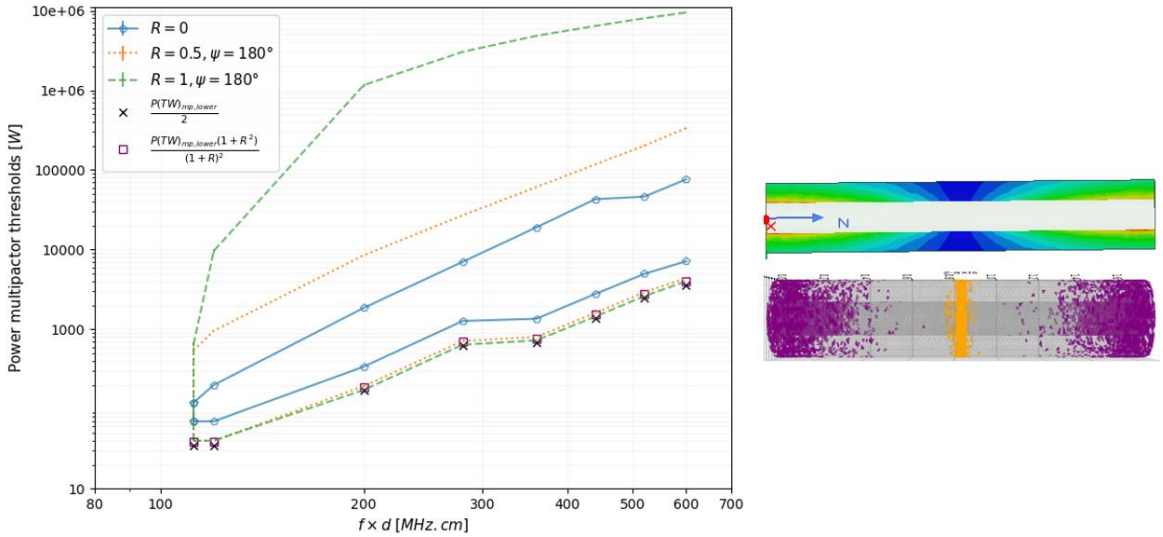

Fig. 5: Left – The blue, orange, and green curves represent respectively the lower and upper power multipactor thresholds for the wave patterns: TW, MW, and SW. The purple and black points represent the expected lower multipactor thresholds for the MW, and SW patterns as suggested by Somersalo. Right – On top the electric field cartography for a SW pattern is plotted, and on bottom the multipactor susceptible regions for the lower and upper power multipactor thresholds are represented respectively in purple and orange.

Bridge

The two different excitations obtained from the circuit analysis of one IC antenna facing vacuum (Table 1) are first normalized to 1W, and then their corresponding electromagnetic cartographies are imported to Spark3D for multipactor

power threshold calculations in each of the predefined regions. It has been found that, at 55 MHz, for the chosen TEEY data curve, no multipactor is observed in regions: A, B, and D. Whereas, the multipactor appears in regions C, E, and F. The lower and upper power multipactor thresholds $(\boldsymbol{P_{mp,lower}}, \boldsymbol{P_{mp,upper}})$ for each of these regions are given in Table 2. On the left hand side of Fig. 7, the electric field cartography for the antenna right-sided bridge's normalized excitations is plotted. On the right, the purple, and orange susceptible regions correspond respectively to the lower $\boldsymbol{P_{mp,lower}}$, and upper $\boldsymbol{P_{mp,upper}}$ power multipactor thresholds are plotted. This evidences that the multipactor ignition is near the maximum of the electric field, whereas, its quenching is near the minimum of the electric field within the same region. The same conclusions were drawn from the analysis of regions E and F. For each bridge excitation (left and right), and in each region, the proposed criterion for the $\boldsymbol{P_{mp,lower}}$ and $\boldsymbol{P_{mp,upper}}$ *i.e.*, $E_{peak}(\boldsymbol{P_{mp,lower}})$ and $E_{mean}(\boldsymbol{P_{mp,upper}})$ are evaluated to check their independence of the geometry's excitations. The obtained values are plotted in Fig. 8 and show that $E_{peak}(\boldsymbol{P_{mp,lower}})$ and $E_{mean}(\boldsymbol{P_{mp,upper}})$, of the left and right port excitations, are almost equal in each of the regions. The percentage difference does not exceed 4%.

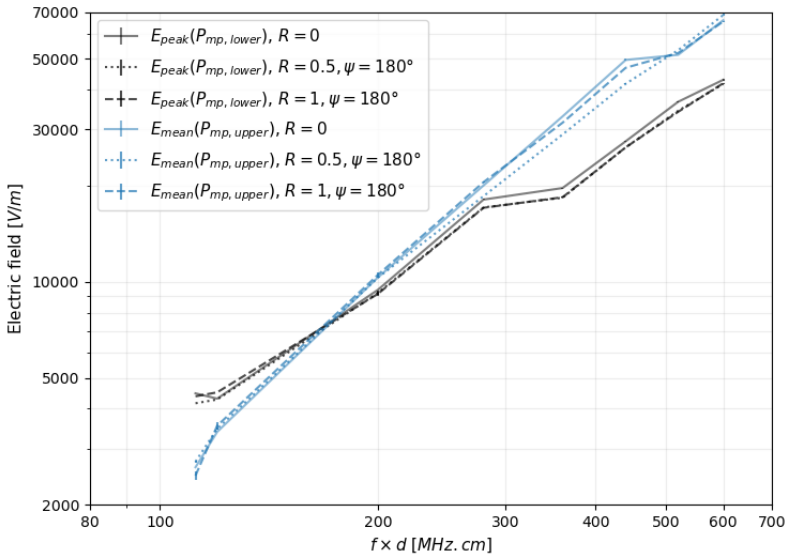

Fig. 6: The solid, dotted and dashed black curves represent the peak electric field corresponding to the lower power multipactor thresholds of respectively the TW, MW, and SW patterns. The solid, dotted and dashed blue curves represent the mean electric field calculated in the multipactor regions and correspond to the upper power multipactor thresholds of respectively the TW, MW, and SW patterns.

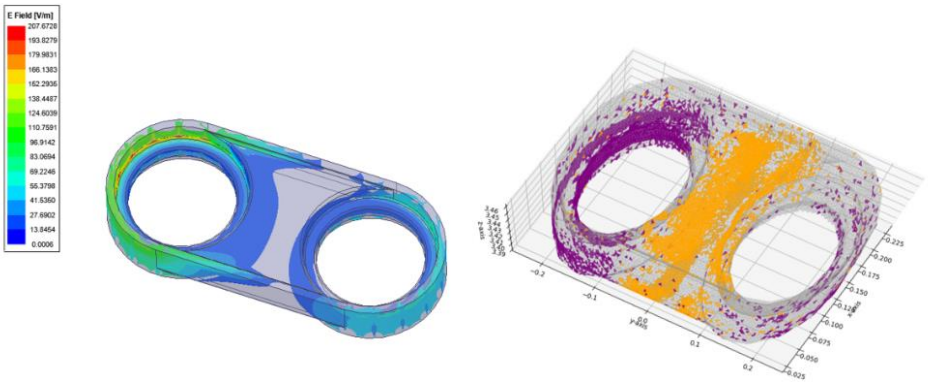

Fig. 7: Left – The electric field cartography in region C, corresponding to the normalized excitations of the right side bridge. Right – The purple and the orange regions correspond respectively to the multipactor susceptible region of the lower, and upper multipactor power thresholds.

Table 2: Power multipactor thresholds for the regions C, E, and F of the bridge geometry of each antenna side.

Bridge	Region C		Region E		Region F	
	$\boldsymbol{P_{mp,lower}}$[W]	$\boldsymbol{P_{mp,upper}}$ [W]	$\boldsymbol{P_{mp,lower}}$[W]	$\boldsymbol{P_{mp,upper}}$[W]	$\boldsymbol{P_{mp,lower}}$[W]	$\boldsymbol{P_{mp,upper}}$[W]
Left	9680	2.58×10^6	1480	19310	660	5053
Right	11323	2.8×10^6	1297	15013	717	5677

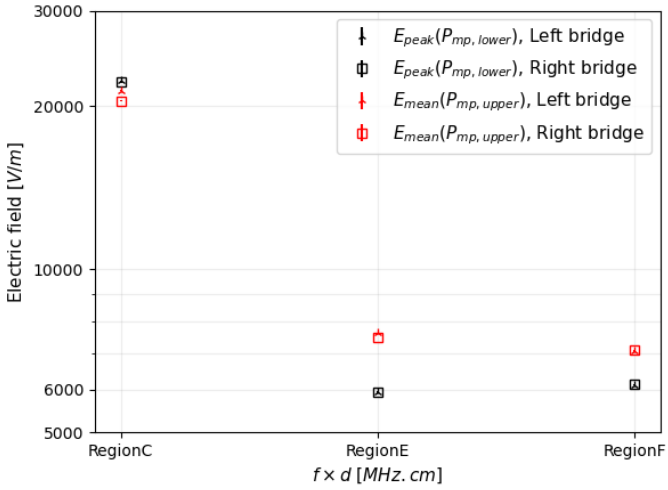

Fig. 8: The black points represent the peak electric field corresponding to the lower power multipactor thresholds of the regions C, E, F for the bridge's left (arrows) and right (squares) antenna excitations. The red points represent the mean electric field corresponding to the upper power multipactor thresholds of the regions C, E, F for the bridge's left (arrows) and right (squares) antenna excitations.

CONCLUSION

In this paper, we have proposed two multipactor-electric field-based criteria for both the lower and upper multipactor thresholds and independently of the ports excitations (wave patterns). The proposed criteria have been validated for two types of geometries: a coaxial line and a complex 3-port geometry, where we have found that independently of the ports excitations the maximum multipactor electric field of the lower power multipactor threshold and the mean multipactor electric field of the upper power multipactor threshold are always the same. Moreover, the results found in this work are in good agreement with the previous findings, in terms of proposed scaling laws for the lower multipactor voltages' independency of the wave patterns, and the sustainability of the multipactor near the nodes of the SW pattern at very high incident powers for a simple coaxial geometry.

REFERENCES

[1] Kishek, "Multipactor discharge on metals and dielectrics: historical review and recent theories," vol. 5, pp. 2120–2126, May 1998.
[2] R. Woo, "Woo 1970_Final report on RF Voltage Breakdown in Coaxial Transmission lines."
[3] GillandVonEngel1948, "Starting potentials of high-frequency gas discharges at low pressure," *Proc. R. Soc. Lond. Ser. Math. Phys. Sci.*, vol. 192, no. 1030, pp. 446–463, Feb. 1948, doi: 10.1098/rspa.1948.0018.
[4] J. R. M. Vaughan, "Multipactor," *IEEE Trans. Electron Devices*, vol. 35, no. 7, pp. 1172–1180, Jul. 1988, doi: 10.1109/16.3387.
[5] T. P. Graves, S. J. Wukitch, B. LaBombard, and I. H. Hutchinson, "Effect of multipactor discharge on Alcator C-Mod ion cyclotron range of frequency heating," *J. Vac. Sci. Technol. Vac. Surf. Films*, vol. 24, no. 3, pp. 512–516, May 2006, doi: 10.1116/1.2194937.
[6] Somersalo, E., "Computational methods for analyzing electron multipacting in RF structures," 1998.
[7] A. M. Perez *et al.*, "Prediction of Multipactor Breakdown Thresholds in Coaxial Transmission Lines for Traveling, Standing, and Mixed Waves," *IEEE Trans. Plasma Sci.*, vol. 37, no. 10, pp. 2031–2040, Oct. 2009, doi: 10.1109/TPS.2009.2028428.
[8] Romanov, Gennady, "Stochastic features of multipactor in coaxial waveguides for travelling and standing waves," 2011.
[9] J. Hillairet, "RF network analysis of the WEST ICRH antenna with the open-source python scikit-RF package," Yogyakarta, Indonesia, 2020, p. 070010. doi: 10.1063/5.0013523.